Original Research

Parametric SCAPS-1D Optimization of CuO Thin Film Solar Cells with CdS, ZnO, and TiO_2 Buffer Layers

Amol C. Badgujar [1,*], Satish R. Patil [1], Nilesh P. Salunke [1]

[1] Department of Mechanical Engineering, SVKM's Institute of Technology Dhule, Dhule 424001, India
* Correspondence: amol.badgujar@svkm.ac.in

Received: December 11, 2025; Accepted: January 28, 2026

Abstract: Copper oxide (CuO) is a stable, earth-abundant p-type semiconductor with strong potential as an absorber material for thin-film solar cells (TFSCs). However, experimentally reported efficiencies for CuO TFSCs remain significantly below theoretical limits, primarily due to interfacial recombination and suboptimal heterojunction design. In this work, a systematic SCAPS-1D numerical investigation of CuO-based TFSCs incorporating CdS, ZnO, and TiO_2 buffer layers is presented. The device architecture, with an Au/CuO/buffer/Al:ZnO/Al configuration, was modeled to simultaneously optimize buffer-layer thickness and donor density, thereby evaluating the coupled geometrical and electronic effects. Unlike prior studies focusing on individual buffer materials or limited parameter spaces, this work provides a unified comparative framework for assessing buffer-layer compatibility with CuO absorbers. The results show that TiO_2 achieves the highest simulated power conversion efficiency of 12.48%, followed by ZnO at 12.00% and CdS at 11.60%. While CdS remains a widely adopted buffer layer in TFSCs, TiO_2 demonstrates improved compatibility with CuO in terms of band alignment, optical transparency, and parameter tolerance. The reported efficiencies represent upper-bound estimates due to idealized interface and optical assumptions inherent to SCAPS-1D simulations; therefore, experimental validation and interface-defect modeling are required to confirm device performance under realistic fabrication conditions.

Keywords: CuO; SCAPS-1D; CdS; ZnO; TiO_2; solar cells

1. Introduction

Solar photovoltaic technology will be a significant contributor to meeting the world's growing energy demands as nations transition away from conventional fossil fuels. Thin film solar cells (TFSCs) will also make a significant contribution in satisfying the needs and have gained substantial interest due to their potential for cost-effective production, mechanical flexibility, and capability for large-area deployment of flexible, lightweight and building-integrated photovoltaics. The conventional TFSC technologies, such as CIGS [1,2] and CdTe [3,4] are mature technologies with efficiencies exceeding 23%. Still, they encounter challenges including complex and expensive manufacturing processes, toxicity, environmental risks, and scarcity of In and Te. Another promising TFSC technology is perovskite-based solar cells, where efficiencies have exceeded 25% but suffer from challenges such as long-term stability and Pb management [5,6]. These limitations with current TFSC technologies have led to the quest for sustainable and earth-abundant alternatives. Copper oxide (CuO) is one such material that has gained attention as a viable absorber due to its inexpensiveness, natural abundance, and favourable optoelectronic properties. CuO is a p-type semiconductor with a bandgap of 1.2–1.5 eV and a high absorption coefficient of over 10^5 cm^{-1}. It can effectively absorb a wide range of the solar spectrum at micrometer thickness [7,8]. The spray

pyrolysis [9], sol-gel processing [10], electrodeposition [11], sputtering [12], and chemical bath [13] techniques have been reported in several experimental studies for preparing CuO thin films with tunable optoelectronic properties, suitable for TFSC applications. However, the reported efficiencies of CuO TFSCs remain relatively low, ranging from 0.02% to 9.3% [14–18], which is significantly below their Shockley–Queisser limit of ~30% [19–21]. The performance of CuO TFSC is strongly influenced by the choice of n-type buffer layer, which governs band alignment, charge separation, and interfacial recombination. Various n-type semiconductors, such as silicon [22], metal oxides [23,24] and metal sulphides [25,26] have been investigated as heterojunction partners for CuO in experimental studies. Buffer materials such as CdS, ZnO, and TiO_2 have been widely explored due to their wide band gaps, high optical transparency, and favorable electronic properties [27–31]. While CdS is a well-established buffer layer in conventional thin-film technologies, oxide buffer layers such as ZnO and TiO_2 offer potential advantages in terms of transparency, chemical stability, and compatibility with oxide absorbers. However, most existing studies examine these buffer materials independently or under differing simulation assumptions, which limits a direct comparison of their relative effectiveness in CuO-based heterojunctions. Numerical simulations using SCAPS-1D offer an efficient method for evaluating inorganic TFSC device designs and adjusting parameters without the need for extensive experimental work [32–35]. Although SCAPS-1D studies on CuO heterojunction solar cells employing CdS, ZnO, or TiO_2 buffer layers have been reported, these investigations typically focus on individual buffer materials, limited parameter variations, or differing simulation assumptions. The present work employs a unified comparative parametric framework in which buffer-layer thickness and donor density are simultaneously optimized for CdS, ZnO, and TiO_2 under identical device architectures and modeling conditions. This approach allows a consistent comparison of buffer-layer compatibility with CuO absorbers. It enables systematic analysis of the influence of band alignment, recombination behavior, and electric field distribution, aspects that have not been jointly examined in prior studies.

2. Materials and methods

This study utilizes numerical simulations with SCAPS-1D (Version: SCAPS 3.8, Release date: May 2020, University of Gent, Belgium) to investigate the performance of CuO TFSCs incorporating buffer layers of CdS, ZnO, and TiO_2. The simulator enables detailed analysis of optoelectronic behaviour, allowing systematic evaluation of material, geometrical, and doping parameters by solving the coupled semiconductor equations [36,37].

Poisson's equation:

$$\frac{d}{dx}\left(\varepsilon_0 \varepsilon_r \frac{d\psi}{dx}\right) = -q(p - n + N_D^+ - N_A^-) \tag{1}$$

Electron continuity equation:

$$\frac{dn}{dt} = \frac{1}{q}\frac{dJ_n}{dx} + G - R \tag{2}$$

Hole continuity equation:

$$\frac{dp}{dt} = -\frac{1}{q}\frac{dJ_p}{dx} + G - R \tag{3}$$

where

ψ is the electrostatic potential,

ε_0 and ε_r are the vacuum and relative dielectric constants,

n and p are carrier concentrations,

N_D and N_A are donor and acceptor densities,

J_n and J_p are current densities, and,

G and R represent generation and recombination rates.

Carrier transport is governed by drift–diffusion currents with mobilities $\mu_{n,p}$ and diffusion coefficients $D_{n,p}$ as follows:

$$J_n = qn\mu_n \frac{d\psi}{dx} + qD_n \frac{dn}{dx} \tag{4}$$

$$J_p = qp\mu_p \frac{d\psi}{dx} - qD_p \frac{dp}{dx} \tag{5}$$

In SCAPS-1D, Poisson's equation is solved self-consistently with the electron and hole continuity equations to describe the electrostatic potential and carrier transport governed by electric-field-driven drift and concentration-gradient-driven diffusion. Recombination is modeled using Shockley–Read–Hall statistics through bulk defect states, which dominate non-radiative recombination in CuO TFSCs, while radiative and Auger recombination mechanisms are neglected.

2.1. Device structure

Figure 1 illustrates the simulated solar cell configuration: Au/CuO/n-type layer/Al:ZnO/Al, which forms the basis for performance evaluation in this study. The device configuration contains CuO as the key absorber layer. The CdS, ZnO, and TiO_2 layers serve as buffer layers that form a p-n junction with the absorber. Al:ZnO acts as a transparent front contact, allowing sunlight into the absorber layer and junctions. Gold is used as a back contact, while the aluminium grid serves as a front contact on the Al:ZnO layer to extract current from the device.

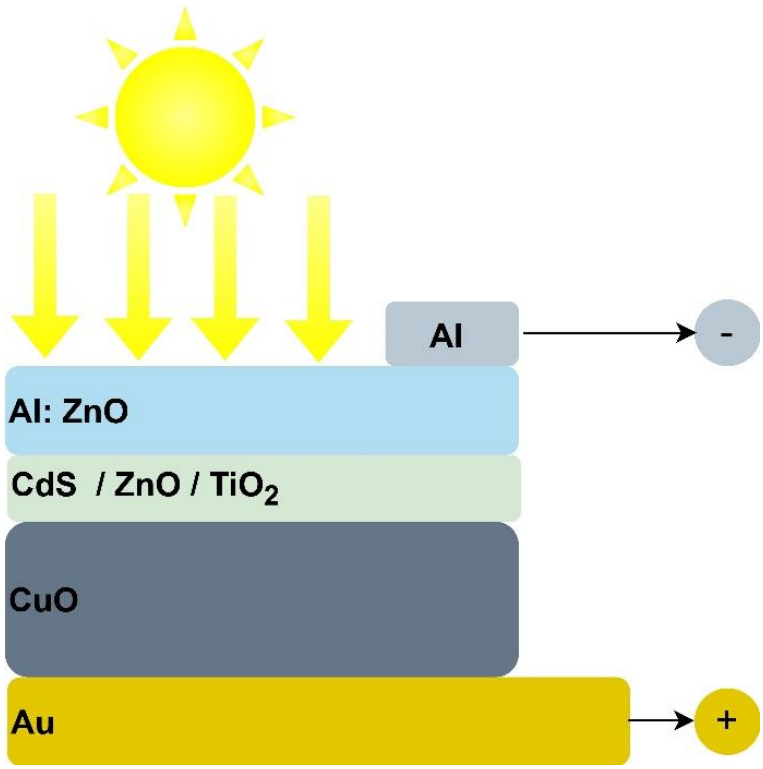

Figure 1. Schematic structure of the simulated CuO TFSC: Au/CuO/buffer layer/Al:ZnO/Al.

2.2. Material properties

All material parameters, including band gaps, electron affinities, dielectric constants, effective density of states, carrier mobilities, and defect densities, were obtained from experimental reports and prior SCAPS-1D studies. These values are summarized in Table 1 [37–56]. Buffer-layer thicknesses were varied in the range of 20–100 nm. The donor density ranges listed in Table 1 were determined based on experimental feasibility. The CuO absorber layer was assigned an acceptor concentration of 10^{16} cm^{-3}, consistent with experimental estimates. All layers, except Al:ZnO,

included a neutral bulk defect level of 10^{15} cm^{-3} to represent deep-level recombination centers. Simulations were conducted under standard AM1.5G illumination (100 mW/cm^2) at 300 K, utilising the default SCAPS-1D optical model. The photovoltaic parameters open-circuit voltage (V_{OC}), short-circuit current density (J_{SC}), fill factor (FF), and power conversion efficiency (η) were extracted. Ideal interfaces were assumed in the simulations to isolate material and geometry-dependent effects and enable direct comparison among buffer layers. In CuO heterojunction devices, reported interface defect densities (~10^{10}–10^{13} cm^{-2}) can reduce absolute efficiencies by approximately 5%–10% due to enhanced recombination. However, prior SCAPS-1D studies show that such defects mainly shift absolute performance values without altering relative trends, justifying the ideal-interface assumption for comparative analysis [30]. Optical generation profiles were calculated using the standard SCAPS-1D optical model under AM1.5G illumination, based on the absorption coefficients of individual layers. Parasitic absorption, reflection losses, and advanced light-trapping effects are not explicitly considered; therefore, the calculated current densities represent upper-bound values. Ohmic contacts were assumed at both electrodes, and interface defect states were neglected to enable a comparative assessment of buffer-layer effects under identical simulation assumptions.

Table 1. Material properties of key layers utilized in the present simulation work acquired from the literature sources [37–56].

Property/Layer	CuO	CdS	ZnO	TiO_2	Al:ZnO
Thickness (nm)	1000	20–100	20–100	20–100	200
Band Gap (eV)	1.2	2.4	3.3	3.2	3.3
Electron Affinity (eV)	4.07	4.40	4.45	3.90	4.40
Dielectric Permittivity	18.1	9.0	9.0	10.0	9.0
CB effective density of States (cm^{-3})	3.0×10^{19}	2.2×10^{18}	2.2×10^{18}	2.0×10^{17}	2.2×10^{18}
VB effective density of States (cm^{-3})	5.5×10^{20}	1.8×10^{18}	1.8×10^{18}	6.0×10^{17}	1.8×10^{18}
Electron mobility (cm^2/Vs)	200	10	100	100	10
Hole mobility (cm^2/Vs)	20	5	25	25	5
Shallow Uniform donor density N_D (cm^{-3})	-	10^{12}–10^{19}	10^{16}–10^{20}	10^{16}–10^{19}	10^{21}
Shallow Uniform acceptor density N_A (cm^{-3})	10^{16}	-	-	-	-
Defect Category	Neutral	Neutral	Neutral	Neutral	-
Defect Density (cm^{-3})	10^{15}	10^{15}	10^{15}	10^{15}	-

3. Results and discussion

This section analyzes the photovoltaic performance of CuO TFSCs with CdS, ZnO, and TiO_2 buffer layers. The effects of buffer layer thickness and donor density on V_{OC}, J_{SC}, FF, and η are assessed using SCAPS-1D. Two-parameter contour maps visualize the effects of electronic and geometrical optimization.

Figure 2 illustrates the effect of CdS layer properties on the device with Au/CuO/CdS/Al:ZnO/Al configuration. The V_{OC} increases gradually with donor density, reaching ~0.48 V at 10^{19} cm^{-3} (Figure 2(a)). This improvement stems from an enhanced built-in potential and reduced recombination in the depletion region. CdS thickness has a weaker effect on V_{OC}, with only marginal enhancement beyond 80 nm. The short-circuit current density, J_{SC}, is more sensitive to both doping and thickness (Figure 2(b)). A higher donor concentration increases the free carrier density and

reduces recombination, resulting in J_{SC} values of up to ~35.85 mA/cm^2. Likewise, thicknesses above 80 nm improve charge collection by decreasing series resistance; however, excessively thick CdS begins to reduce optical transmission. The fill factor exhibits a monotonic rise with donor density (Figure 2(c)), reaching ~70.40% at high doping. This is attributed to improved conductivity and reduced series resistance. CdS thickness exhibits a secondary influence; gains diminish beyond 80–100 nm, as additional thickness contributes resistive losses without offering a significant optical benefit. The efficiency map (Figure 2(d)) reveals an optimal region with a thickness of ~80–100 nm and a donor density of around 10^{19} cm^{-3}, where η reaches ~11.60%. Increasing either parameter beyond this range yields diminishing returns due to the trade-off between optical transparency and resistive losses. Overall, CdS-based devices demonstrate reasonable performance but require high doping levels that are difficult to achieve experimentally through conventional chemical bath methods.

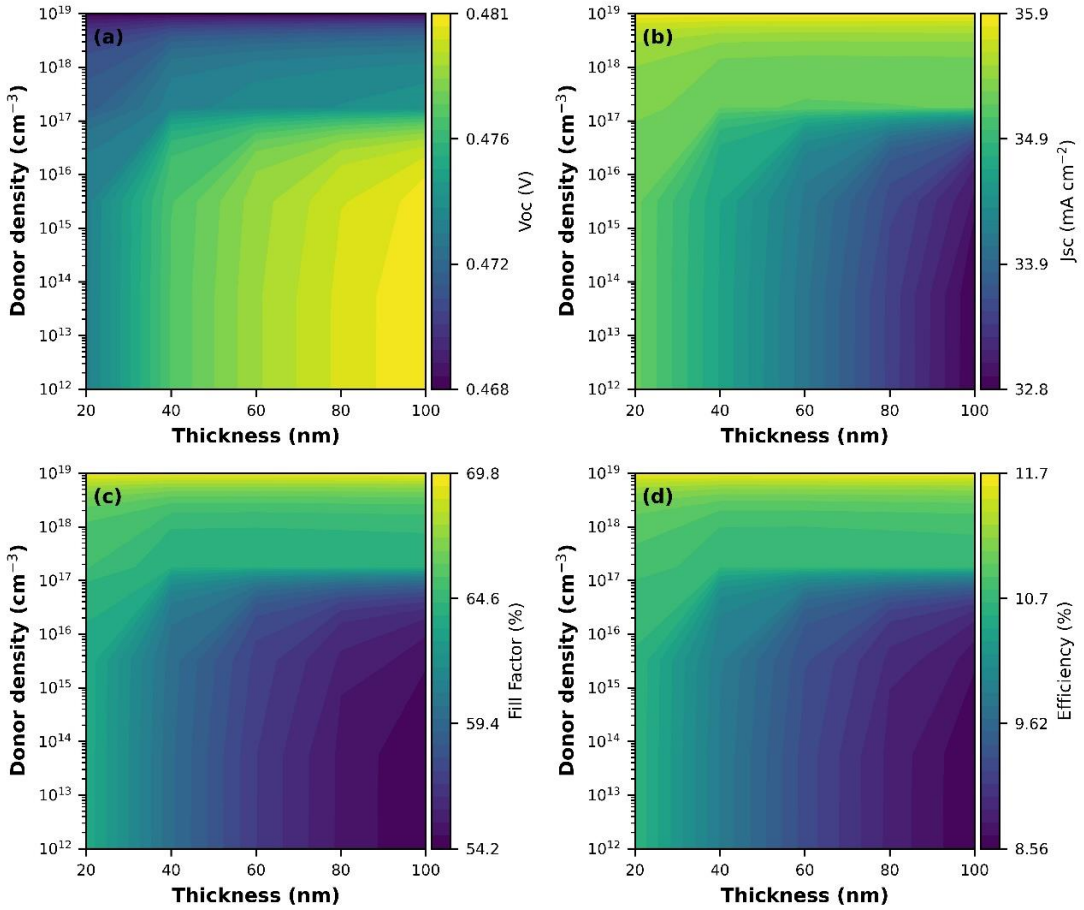

Figure 2. Contour maps for CuO/CdS/Al:ZnO/Al solar cells showing the effect of CdS thickness (20–100 nm) and donor density (10^{12}–10^{19} cm^{-3}) on (a) V_{OC}; (b) J_{SC}; (c) FF; and (d) η.

Figure 3 illustrates the effect of ZnO layer properties on device output. V_{OC} increases moderately with donor density up to ~0.48 V (Figure 3(a)), a result of the strengthened electric field and reduced depletion-region recombination. Similar to CdS, V_{OC} saturates as the thickness exceeds ~80 nm. J_{SC} demonstrates stronger dependence on both parameters (Figure 3(b)). Peak J_{SC} values of ~36.00 mA/cm^2 are observed at high donor densities (10^{20} cm^{-3}), reflecting improved carrier extraction efficiency. Increasing ZnO thickness from 20 to 100 nm also enhances J_{SC} by reducing series resistance. However, the optical penalty becomes noticeable beyond ~100 nm. The fill factor improves significantly with donor concentration, reaching 69.60% under heavy doping (Figure 3(c)). This behavior is consistent with improved carrier mobility and reduced resistive losses. The dependence on thickness is moderate, with noticeable improvement between 40 and 80 nm. The efficiency contour

(Figure 3(d)) indicates an optimal region with a thickness of 80–100 nm and a donor density of 10^{20} cm^{-3}, yielding an η of approximately 12.00%. The broader, plateau-like contour region indicates that ZnO-based devices are less sensitive to thickness variations than CdS-based devices. Thus, ZnO represents a more fabrication-tolerant heterojunction partner.

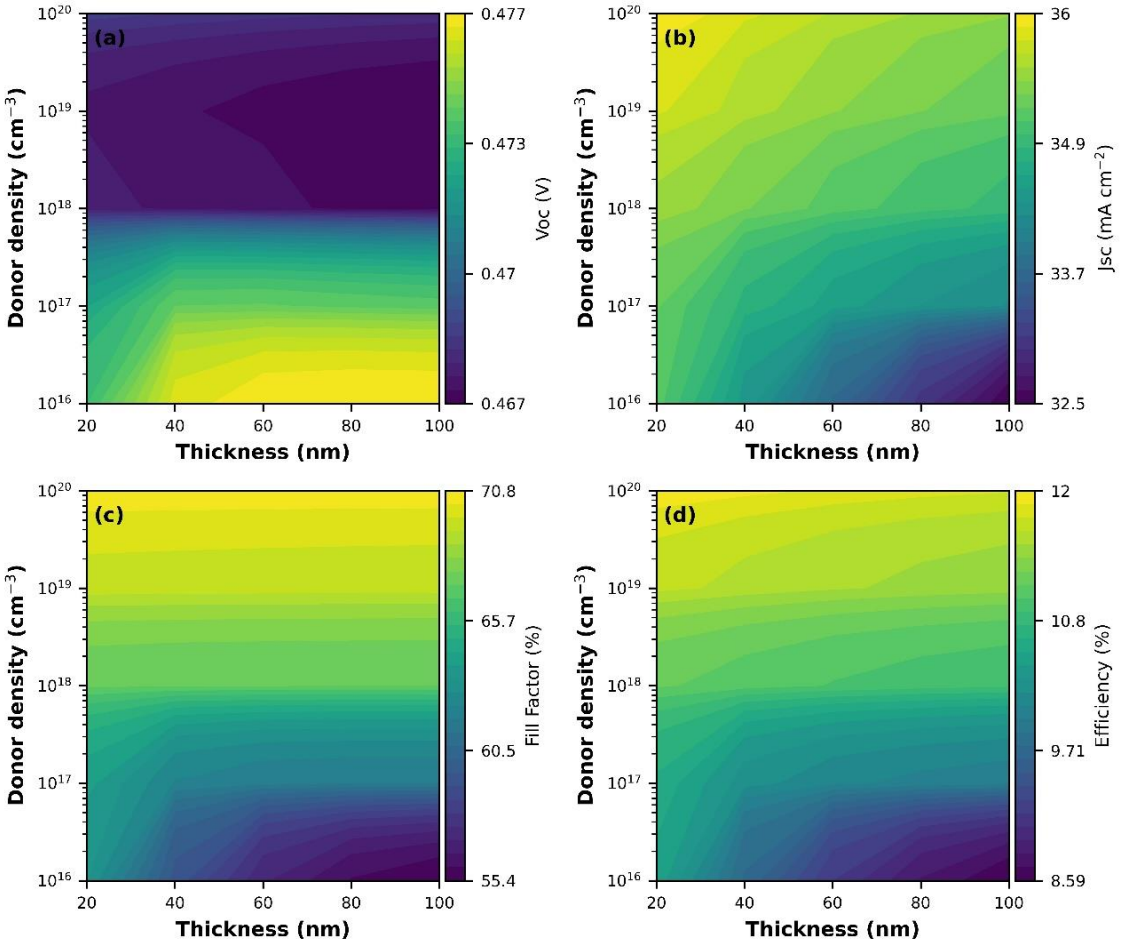

Figure 3. Contour maps for CuO/ZnO/Al:ZnO/Al solar cells illustrating the influence of ZnO thickness (20–100 nm) and donor density (10^{16}–10^{20} cm^{-3}) on (a) V_{OC}; (b) J_{SC}; (c) FF; and (d) η.

Figure 4 presents the contour maps for the CuO/TiO_2 configuration, which exhibits the highest performance among the three systems. V_{OC} increases steadily with donor density (10^{16}–10^{19} cm^{-3}), reaching ~0.47 V (Figure 4(a)). The limited sensitivity to TiO_2 thickness suggests that voltage is primarily dominated by band alignment and the doping-induced electric field. J_{SC} exhibits a strong and nearly linear dependence on both parameters (Figure 4(b)). Higher donor density increases band bending at the heterojunction, strengthening carrier separation and enabling J_{SC} values up to ~36.50 mA/cm^2. The moderate refractive index and wide bandgap of TiO_2 allow high optical transparency even at increased thickness, which contributes to improved photocurrent. The fill factor reaches ~72.60% at high donor density (Figure 4(c)), the highest among all three devices. This enhancement stems from reduced series resistance and favourable electron transport properties associated with the relatively high mobility and wide bandgap of TiO_2. The efficiency contour (Figure 4(d)) indicates a maximum η of 12.48% at a thickness of ~80–100 nm and a donor density of 10^{19} cm^{-3}. Notably, the TiO_2 region shows more stable performance across a broader parameter range compared to CdS and ZnO. This robustness is linked to more favourable conduction-band offset and reduced interfacial recombination, as predicted for CuO/TiO_2 heterojunctions.

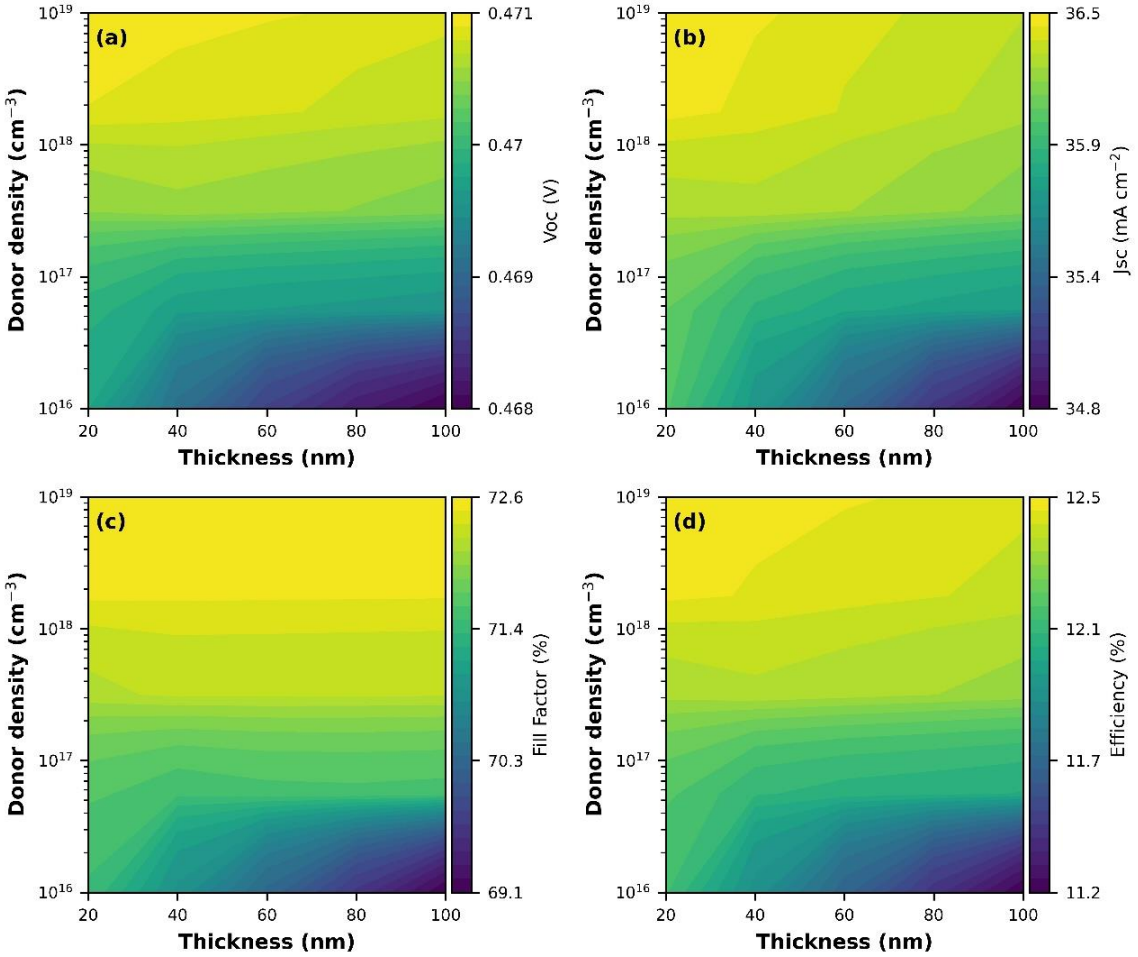

Figure 4. Contour maps for CuO/TiO_2/Al:ZnO/Al solar cells showing the effect of TiO_2 thickness (20–100 nm) and donor density (10^{16}–10^{19} cm^{-3}) on (a) V_{OC}; (b) J_{SC}; (c) *FF*; and (d) η.

Figure 5 compares the I–V curves of the three optimized devices. The differences in V_{OC} and *FF* are modest, whereas the improvement in TiO_2-based devices is primarily attributable to enhanced carrier collection and reduced recombination. Given its very wide bandgap (~3.2 eV), TiO_2 transmits more high-energy photons to the CuO absorber, enabling a higher photogeneration rate than CdS or ZnO. The superior performance of the CuO/TiO_2 device can be further understood from the band-alignment analysis shown in Figure 6, where a small conduction-band spike reduces interface recombination compared to the conduction-band cliffs observed in CuO/CdS and CuO/ZnO heterojunctions. Within the SCAPS-1D drift–diffusion framework, increasing the buffer-layer donor density strengthens band bending and the built-in electric field, improving carrier separation and reducing recombination losses in the depletion region.

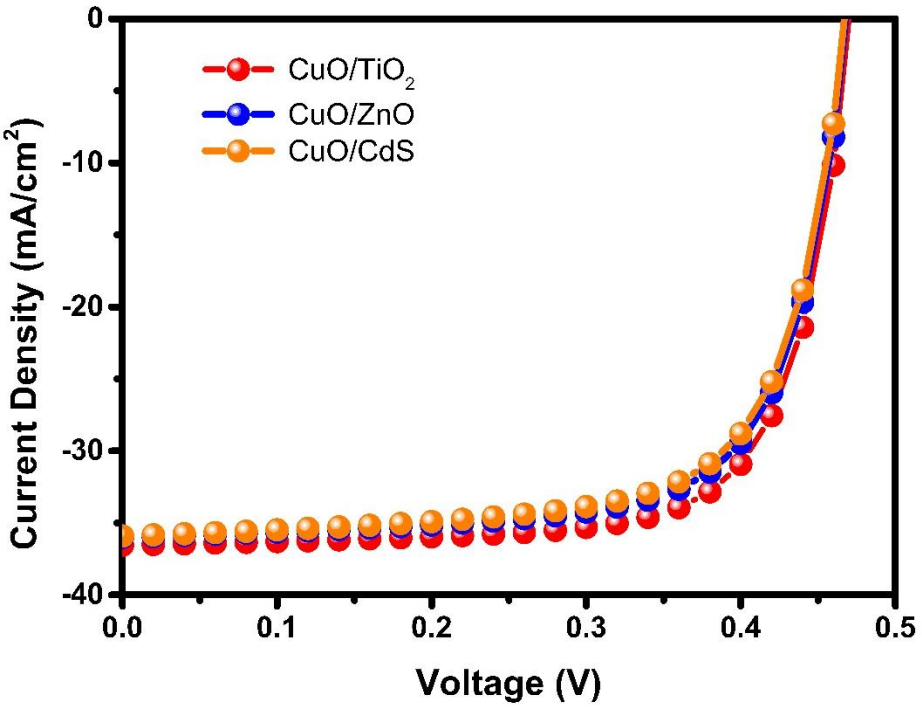

Figure 5. Current–voltage (I–V) characteristics of optimized CuO TFSCs using CdS, ZnO, and TiO_2 buffer layers under AM1.5G illumination.

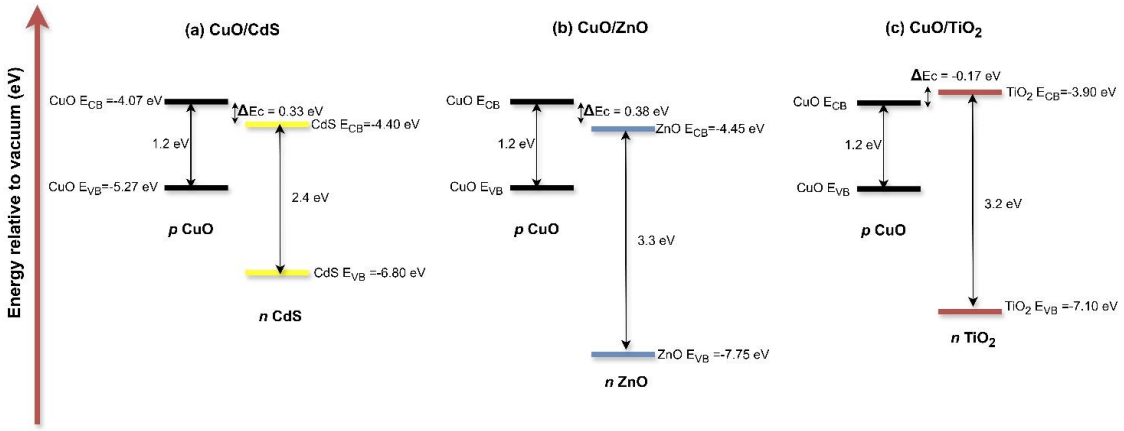

Figure 6. Band alignment diagrams of (a) CuO/CdS; (b) CuO/ZnO; (c) CuO/TiO_2 heterojunctions derived from electron-affinity values.

CdS is a well-established and widely used buffer layer in thin-film solar cells, owing to its favorable electrical properties and demonstrated high performance in technologies such as CdTe and CIGS. However, the suitability of the buffer layer is strongly dependent on the absorber. Although CdS based solar cells also demonstrated fair efficiencies, preparing CdS thin films with donor densities of 10^{19} cm^{-3} by the conventional chemical bath route is challenging. Doping CdS thin films beyond a specific limit tends to form degenerate semiconductors [48]. ZnO and TiO_2 offer greater flexibility in achieving high donor concentrations. For ZnO, donor densities in the range of ~10^{16}–10^{20} cm^{-3} have been experimentally reported earlier [43,55,56] through Al or Ga doping and oxygen vacancy engineering, which overlap well with the optimal ranges identified in the present simulations. Similarly, TiO_2 can exhibit donor densities on the order of ~10^{17}–10^{19} cm^{-3} [51–53] via oxygen deficiency or aliovalent doping, consistent with the simulated optimal values. These considerations suggest that, compared to CdS, ZnO and TiO_2 are more practically compatible with the donor density requirements predicted by the numerical optimization. Overall variation in

performance in the case of TiO_2-based buffer layer is robust to variations in buffer layer thickness and donor density. Although SCAPS-1D simulations predict a high efficiency of 12.48%, experimental validation of such devices remains limited due to several fabrication challenges. One key issue is the control over the interface quality between CuO and TiO_2, where lattice mismatch and defect states can severely degrade performance. Additionally, deposition techniques such as reactive sputtering and sol-gel processing must be carefully tuned to achieve uniform TiO_2 layers with the desired doping concentrations and thicknesses. Recent experimental efforts have reported CuO/TiO_2 heterojunction solar cells with efficiencies of approximately 9% [18], reflecting both the potential and the gap between idealized simulations and actual devices. Interface passivation, surface treatment, and doping control are active areas of research aimed at improving real-world performance [57–60]. Hence, while TiO_2 remains the most promising buffer layer in simulation, overcoming practical limitations through advanced fabrication techniques is essential for its successful implementation. Beyond optoelectronic performance, environmental and stability considerations play a crucial role in selecting materials for scalable photovoltaic applications. CdS, while commonly used as a buffer layer, poses serious environmental as well as health hazards due to cadmium toxicity and its potential for leaching, particularly during large-scale fabrication and disposal [61,62]. In contrast, TiO_2 and ZnO are widely regarded as environmentally benign, earth-abundant, and chemically stable. TiO_2, in particular, is non-toxic and exhibits superior resistance to photo as well as thermal degradation, making it more suitable for long-term deployment. ZnO, though more environmentally friendly than CdS, may suffer from chemical instability under acidic or humid conditions. These comparative advantages strengthen the case for TiO_2 as a safer and more sustainable alternative in CuO-based TFSCs, particularly in contexts that demand green manufacturing and ecological compliance.

4. Limitations

The present work is based on SCAPS-1D numerical simulations and is therefore subject to several inherent limitations. Ideal interfaces between CuO and the buffer layers are assumed, while interface defect states that commonly occur in experimentally fabricated devices are not considered. Such defects can introduce additional recombination pathways, thereby reducing the absolute device performance. Nevertheless, earlier numerical studies indicate that these effects mainly influence absolute efficiency values rather than the relative trends among different buffer materials [30], which is the primary focus of this study.

The SCAPS-1D optical model neglects parasitic absorption, reflection losses, and incomplete light trapping within the device stack. Consequently, the calculated short-circuit current densities should be interpreted as upper-bound estimates rather than direct experimental values. Additionally, some donor density values explored in the simulations correspond to theoretical or near-ideal limits, intended to assess performance trends. Their experimental realization may require advanced doping strategies and precise process control.

Moreover, numerical simulations do not capture fabrication-related non-uniformities, interface roughness, or the effects of long-term stability and degradation. Accordingly, while this work provides a comparative and physically motivated framework for buffer-layer selection and optimization in CuO, experimental validation remains essential to confirm the predicted performance under realistic operating conditions.

5. Conclusions

This work presented a systematic SCAPS-1D simulation study of CuO TFSCs employing CdS, ZnO, and TiO_2 buffer layers, with simultaneous optimization of buffer-layer thickness and donor density under identical modeling assumptions. The comparative analysis revealed that device performance is strongly governed by interfacial band alignment, recombination behavior at the CuO/buffer heterojunction. Among the three configurations, CuO/TiO_2 achieved the highest efficiency of 12.48%, followed by 12.00% for CuO/ZnO and 11.60% for CuO/CdS. The CuO/TiO_2 heterojunction forms a small conduction-band spike that suppresses interfacial recombination while maintaining efficient electron transport, whereas CuO/CdS and CuO/ZnO interfaces form

conduction-band cliffs that enhance recombination losses. While CdS remains a proven and widely adopted buffer layer in TFSCs, the present results indicate that TiO_2 offers distinct advantages for CuO-based devices, particularly in terms of band-alignment compatibility and parameter tolerance. Overall, this study establishes a unified physical framework for buffer-layer selection in CuO TFSCs and highlights TiO_2 as a promising buffer material for CuO absorbers. Building on these insights, future studies that integrate interface defect modeling and experimental validation are expected to further enhance device performance.

Acknowledgments: The authors would like to express sincere gratitude to Marc Burgelman from Ghent University for providing access to the SCAPS simulation software. The software has greatly facilitated the modelling and analysis of solar cell structures, allowing for detailed performance evaluation and optimization.

Declaration of AI and AI-Assisted Technologies in the Writing Process: All authors acknowledge the responsible use of Artificial Intelligence-based tools, such as ChatGPT and Grammarly, for English language editing and enhancing reader comprehension.

Availability of Data and Materials: The datasets used/developed in the present study are available upon reasonable request to the corresponding author.

Funding: This research received no external funding.

Author Contributions: Conceptualization, AB; methodology, AB; software, AB; validation, AB; formal analysis, AB; investigation, AB, SP and NS; resources, NS; data curation, AB; writing—original draft preparation, AB; writing—review and editing, AB, SP and NS; visualization, AB; supervision, NS; project administration, AB. All authors have read and agreed to the published version of the manuscript. All authors have read and approved the final manuscript. All authors contributed to editorial changes in the manuscript. All authors have participated sufficiently in the work and agreed to be accountable for all aspects of the work.

Conflicts of Interest: The author declare no conflict of interest.

References

1. Buldu, D.G.; de Wild, J.; Kohl, T.; et al. A Novel Strategy for the Application of an Oxide Layer to the Front Interface of Cu(In,Ga)Se_2 Thin Film Solar Cells: Al_2O_3/HfO_2 Multi-Stack Design With Contact Openings. *IEEE Journal of Photovoltaics* 2022, 12(1), 301–308. https://doi.org/10.1109/JPHOTOV.2021.3120515
2. Badgujar, A.C.; Dusane, R.O.; Dhage, S.R. Solution-processed CIGS thin film solar cell by controlled selenization process. *Materials Today Proceedings* 2022, 52, 829–833. https://doi.org/10.1016/j.matpr.2021.10.215
3. Bastola, E.; Phillips, A.B.; Barros-King, G.; et al. Understanding the Interplay Between CdSe Thickness and Cu Doping Temperature in CdSe/CdTe Devices. *IEEE Journal of Photovoltaics* 2022, 12(1), 11–15. https://doi.org/10.1109/JPHOTOV.2021.3110338
4. Kuciauskas, D.; Li, S.; Moseley, J.; et al. Voltage Loss Comparison in CdSe/CdTe Solar Cells and Polycrystalline CdSeTe Heterostructures. *IEEE Journal of Photovoltaics* 2022, 12(1), 6–10. https://doi.org/10.1109/JPHOTOV.2021.3117914
5. Fan, T.J.; Xu, W.Z.; Gao, Y.; et al. Antisolvents Treatment of $Cs_{0.15}FA_{0.85}PbI_3$ Boosting Efficiency for Perovskite Solar Cells. *IEEE Journal of Photovoltaics* 2022, 12(1), 322–326. https://doi.org/10.1109/JPHOTOV.2021.3127987
6. Noman, M.; Khan, Z.; Jan, S.T. A comprehensive review on the advancements and challenges in perovskite solar cell technology. *RSC Advances* 2024, 14(8), 5085–5131. https://doi.org/10.1039/D3RA07518D
7. Rakhshani, A.E. Preparation, characteristics and photovoltaic properties of cuprous oxide—a review. *Solid-State Electron* 1986, 29(1), 7–17. https://doi.org/10.1016/0038-1101(86)90191-7
8. Lim, Y.F.; Chua, C.S.; Lee, C.J.J.; et al. Sol–gel deposited Cu_2O and CuO thin films for photocatalytic water splitting. *Physical Chemistry Chemical Physics* 2014, 16(47), 25928–25934. https://doi.org/10.1039/C4CP03241A
9. Abdel-Galil, A.; Moussa, N.L. Nanostructure CuO thin film deposited by spray pyrolysis for technological applications. *Radiation Physics and Chemistry* 2023, 212, 111119. https://doi.org/10.1016/j.radphyschem.2023.111119

10. Anitha, T.V.; Menon, G.K.; Venugopal, K.; et al. Investigating the role of film thickness on the physical properties of sol–gel coated CuO thin films: Discussing its potentiality in optoelectronic applications. *Materials Science and Engineering: B* 2024, 299, 116960. https://doi.org/10.1016/j.mseb.2023.116960
11. Ismail, W.; Bakry, M.; Ibrahim, G.; et al. Impact of bath temperature on the optical, structural, and photoelectrochemical properties of thin films of copper (II) oxide synthesized via electrodeposition method. *Ceramics International* 2025, 51(3), 3423–3431. https://doi.org/10.1016/j.ceramint.2024.11.319
12. Sai Krishna, A.M.; Busi, K.B.; Ramasubramanian, B.; et al. Sputter grown CuO thin films: Impact of growth pressure and annealing temperature on their microstructural architectures. *Memories – Materials, Devices, Circuits and Systems* 2024, 7, 100100. https://doi.org/10.1016/j.memori.2024.100100
13. Jabreen, L.; Mastai, Y. Induced chirality in CuO nanostructures using amino acid-mediated chemical bath deposition. *Crystals* 2025, 15(3), 236. https://doi.org/10.3390/cryst15030236
14. Hussain, S.; Cao, C.; Nabi, G.; et al. Optical and electrical characterization of ZnO/CuO heterojunction solar cells. *Optik* 2017, 130, 372–377. https://doi.org/10.1016/j.ijleo.2016.10.099
15. Bhaumik, A.; Haque, A.; Karnati, P.; et al. Copper oxide based nanostructures for improved solar cell efficiency. *Thin Solid Films* 2014, 572, 126–133. https://doi.org/10.1016/j.tsf.2014.09.056
16. Dolai, S.; Dey, R.; Hussain, S.; et al. Photovoltaic properties of F:SnO_2/CdS/CuO/Ag heterojunction solar cell. *Materials Research Bulletin* 2019, 109, 1–9. https://doi.org/10.1016/j.materresbull.2018.09.022
17. Singh, R.; Alapatt, G.F.; Lakhtakia, A. Making Solar Cells a Reality in Every Home: Opportunities and Challenges for Photovoltaic Device Design. *IEEE Journal of the Electron Devices Society* 2013, 1(6), 129–144. https://doi.org/10.1109/JEDS.2013.2280887
18. Mahmoudabadi, Z.D.; Eslami, E. One-step synthesis of CuO/TiO_2 nanocomposite by atmospheric microplasma electrochemistry—Its application as photoanode in dye-sensitized solar cell. *Journal of Alloys and Compounds* 2019, 793, 336–342. https://doi.org/10.1016/j.jallcom.2019.04.185
19. Shockley, W.; Queisser, H.J. Detailed Balance Limit of Efficiency of p-n Junction Solar Cells. *Journal of Applied Physics* 1961, 32(3), 510–519. https://doi.org/10.1063/1.1736034
20. Ahmmed, S.; Aktar, A.; Tabassum, S.; et al. CuO based solar cell with V_2O_5 BSF layer: Theoretical validation of experimental data. *Superlattices and Microstructures* 2021, 151, 106830. https://doi.org/10.1016/j.spmi.2021.106830
21. Kaphle, A.; Echeverria, E.; Mcllroy, D.N.; et al. Enhancement in the performance of nanostructured CuO–ZnO solar cells by band alignment. *RSC Advances* 2020, 10(13), 7839–7854. https://doi.org/10.1039/C9RA10771A
22. Zenaidi, I.; Bouacheria, M.A.; Djelloul, A.; et al. Preparation and Characterization of Ag/CuO/n-Si/Ag Heterojunction Diode by Sol–Gel DIP-Coating Technique. *Semiconductors* 2024, 58(12), 919–927. https://doi.org/10.1134/S1063782624602309
23. Hasan, S.F.; Fahad, O.A.; Al-Jenaby, A.Z.; et al. High performances multi-function of FTO/ZnO/CuO/Al Heterojunction device: Gas sensor and solar cell. *Journal of Optics* 2024. https://doi.org/10.1007/s12596-024-02349-0
24. Ashok, A.; Jeba Beula, R.; Magesh, R.; et al. Bandgap engineering of CuO/TiO_2 nanocomposites and their synergistic effect on the performance of dye-sensitized solar cells. *Optical Materials* 2024, 148, 114896. https://doi.org/10.1016/j.optmat.2024.114896
25. Nkhaili, L.; El Aakib, H.; Liang, C.T.; et al. A Newly Designed ZnO/CdS/CuO:Co Solar Cell and Its Performance. *Journal of Solar Energy Engineering* 2021, 143(4), 041001. https://doi.org/10.1115/1.4048791
26. El-Naggar, A.A.; Lotfy, L.A.; Felfela, A.A.; et al. Numerical simulation based performance enhancement approach for an inorganic $BaZrS_3$/CuO heterojunction solar cell. *Scientific Reports* 2024, 14(1), 7614. https://doi.org/10.1038/s41598-024-57636-4
27. Roy, A.; Majumdar, A. Optimization of CuO/CdTe/CdS/TiO_2 solar cell efficiency: A numerical simulation modeling. *Optik* 2022, 251, 168456. https://doi.org/10.1016/j.ijleo.2021.168456
28. Lam, N.D. Modelling and numerical analysis of ZnO/CuO/Cu_2O heterojunction solar cell using SCAPS. *Engineering Research Express* 2020, 2(2), 025033. https://doi.org/10.1088/2631-8695/ab9716
29. Husna, J.; Menon, P.S.; Chelvanathan, P.; et al. Numerical study of semi-transparent thin film heterojunction p-CuO/nZnO/AZO/ITO solar cells device model using SCAPS-1D. *Chalcogenide Letters* 2021, 18(11), 667–679. https://doi.org/10.15251/CL.2021.1811.667
30. Sawicka-Chudy, P.; Starowicz, Z.; Wisz, G.; et al. Simulation of TiO_2/CuO solar cells with SCAPS-1D software. *Materials Research Express* 2019, 6(8), 085918. https://doi.org/10.1088/2053-1591/ab22aa

31. Benaissa, N.; Garmim, T.; El Boughdadi, M.; et al. Experimental and numerical simulation studies of CuO thin films based solar cells. *Engineering Research Express* 2023, 5(4), 045038. https://doi.org/10.1088/2631-8695/ad05b3
32. Decock, K.; Khelifi, S.; Burgelman, M. Modelling multivalent defects in thin film solar cells. *Thin Solid Films* 2011, 519(21), 7481–7484. https://doi.org/10.1016/j.tsf.2010.12.039
33. Decock, K.; Zabierowski, P.; Burgelman, M. Modeling metastabilities in chalcopyrite-based thin film solar cells. *Journal of Applied Physics* 2012, 111(4), 043703. https://doi.org/10.1063/1.3686651
34. Burgelman, M.; Decock, K.; Khelifi, S.; et al. Advanced electrical simulation of thin film solar cells. *Thin Solid Films* 2013, 535, 296–301. https://doi.org/10.1016/j.tsf.2012.10.032
35. Burgelman, M.; Nollet, P.; Degrave, S. Modelling polycrystalline semiconductor solar cells. *Thin Solid Films* 2000, 361–362, 527–532. https://doi.org/10.1016/S0040-6090(99)00825-1
36. Manjunath, V.; Reddy, Y.K.; Bimli, S.; et al. 22% efficient Kusachiite solar cells of $CuBi_2O_4$ light harvester and ABO_3 buffer layers: A theoretical analysis. *Materials Today Communications* 2022, 32, 104061. https://doi.org/10.1016/j.mtcomm.2022.104061
37. Sliti, N.; Touihri, S.; Nguyen, N.D. Numerical modeling and analysis of AZO/Cu_2O transparent solar cell with a TiO_2 buffer layer. *Engineering Research Express* 2023, 5(2), 025013. https://doi.org/10.1088/2631-8695/accacf
38. Al-Hattab, M.; Moudou, L.; Khenfouch, M.; et al. Numerical simulation of a new heterostructure CIGS/GaSe solar cell system using SCAPS-1D software. *Solar Energy* 2021, 227, 13–22. https://doi.org/10.1016/j.solener.2021.08.084
39. Karthick, S.; Velumani, S.; Bouclé, J. Chalcogenide $BaZrS_3$ perovskite solar cells: A numerical simulation and analysis using SCAPS-1D. *Optical Materials* 2022, 126, 112250. https://doi.org/10.1016/j.optmat.2022.112250
40. Nezar, S.; Saoula, N.; Sali, S.; et al. Properties of TiO_2 thin films deposited by rf reactive magnetron sputtering on biased substrates. *Applied Surface Science* 2017, 395, 172–179. https://doi.org/10.1016/j.apsusc.2016.08.125
41. Madera, R.G.B.; Nagai, H.; Onuma, T.; et al. Deposition of ZnO and Al-doped ZnO thin films using pressed-sintered targets. *Physica B: Condensed Matter* 2025, 698, 416733. https://doi.org/10.1016/j.physb.2024.416733
42. Look, D.C.; Leedy, K.D.; Tomich, D.H.; et al. Mobility analysis of highly conducting thin films: Application to ZnO. *Applied Physics Letters* 2010, 96(6), 062102. https://doi.org/10.1063/1.3310043
43. Aloui, M.; Mentar, L.; Beniaiche, A.; et al. Electrochemical and physical properties of ZnO nanosheets and ZnO nanowires, under different applied current densities and deposition approaches. *Applied Physics A* 2022, 128(4), 278. https://doi.org/10.1007/s00339-022-05389-0
44. Badgujar, A.C.; Yadav, B.S.; Jha, G.K.; et al. Room Temperature Sputtered Aluminum-Doped ZnO Thin Film Transparent Electrode for Application in Solar Cells and for Low-Band-Gap Optoelectronic Devices. *ACS Omega* 2022, 7(16), 14203–14210. https://doi.org/10.1021/acsomega.2c00830
45. Dhage, S.R.; Badgujar, A.C. Transparent conducting Al:ZnO thin films on large area by efficient cylindrical rotating DC magnetron sputtering. *Journal of Alloys and Compounds* 2018, 763, 504–511. https://doi.org/10.1016/j.jallcom.2018.05.234
46. Sawicka-Chudy, P.; Sibiński, M.; Wisz, G.; et al. Numerical analysis and optimization of Cu_2O/TiO_2, CuO/TiO_2, heterojunction solar cells using SCAPS. *Journal of Physics: Conference Series* 2018, 1033, 012002. https://doi.org/10.1088/1742-6596/1033/1/012002
47. Qu, J.J.; Zhang, L.R.; Wang, H.; et al. Simulation of double buffer layer on CIGS solar cell with SCAPS software. *Optical and Quantum Electronics* 2019, 51(12), 383. https://doi.org/10.1007/s11082-019-2100-9
48. Munaga, V.V.P.; Thyagarajan, K.; Borra, R.K. Structural, surface morphological, optical and thermoelectric properties of sol–gel spin coated Zn doped CdS thin films. *SN Applied Sciences* 2020, 2(4), 552. https://doi.org/10.1007/s42452-020-2358-3
49. Ismail, W.; Ibrahim, G.; Habib, M.A.; et al. Advancement of Physical and Photoelectrochemical Properties of Nanostructured CdS Thin Films toward Optoelectronic Applications. *Nanomaterials* 2023, 13(11), 1764. https://doi.org/10.3390/nano13111764
50. Yılmaz, S. The investigation of spray pyrolysis grown CdS thin films doped with flourine atoms. *Applied Surface Science* 2015, 357, 873–879. https://doi.org/10.1016/j.apsusc.2015.09.098
51. Radecka, M. TiO_2 for photoelectrolytic decomposition of water. *Thin Solid Films* 2004, 451–452, 98–104. https://doi.org/10.1016/j.tsf.2003.11.061

52. Ishizawa, A.; Aizawa, H.; Isshiki, H.; et al. A significant increase in carrier concentration in TiO_2 by Sm doping. *Japanese Journal of Applied Physics* 2024, 63(3), 03SP79. https://doi.org/10.35848/1347-4065/ad2aa1
53. Kompa, A.; U, C.; Kekuda, D.; et al. Investigation on structural, optical and electrical properties of Nd doped titania films and application of optical model. *Materials Science in Semiconductor Processing* 2021, 121, 105293. https://doi.org/10.1016/j.mssp.2020.105293
54. Pham, A.T.T.; Truong, D.C.; Phan, T.T.T.; et al. Tailoring stress relaxation for dopant-free ZnO thin films with high thermoelectric power factor. *Applied Physics Letters* 2024, 124(14), 143901. https://doi.org/10.1063/5.0198063
55. Üzar, N.; Abdulaziz, U. Investigation of the effects of coating numbers of thin films and metal contact type on physical properties of undoped ZnO, Fe-doped ZnO, and Fe–B co-doped ZnO thin films. *Journal of Materials Science: Materials in Electronics* 2024, 35(17), 1136. https://doi.org/10.1007/s10854-024-12817-9
56. Shukla, V.; Patel, A. Effect of doping concentration on optical and electrical properties of intrinsic n-type ZnO (i-ZnO) and (Cu, Na and K) doped p-type ZnO thin films grown by chemical bath deposition method. *Nanosystems: Physics, Chemistry, Mathematics* 2020, 11(4), 391–400. https://doi.org/10.17586/2220-8054-2020-11-4-391-400
57. Sun, H.; Xie, D.Y.; Song, Z.; et al. Interface Defects Passivation and Conductivity Improvement in Planar Perovskite Solar Cells Using Na_2S-Doped Compact TiO_2 Electron Transport Layers. *ACS Applied Materials & Interfaces* 2020, 12(20), 22853–22861. https://doi.org/10.1021/acsami.0c03180
58. Roose, B.; Pathak, S.; Steiner, U. Doping of TiO_2 for sensitized solar cells. *Chemical Society Reviews* 2015, 44(22), 8326–8349. https://doi.org/10.1039/C5CS00352K
59. Richards, B.S.; Cotter, J.E.; Honsberg, C.B. Enhancing the surface passivation of TiO_2 coated silicon wafers. *Applied Physics Letters* 2002, 80(7), 1123–1125. https://doi.org/10.1063/1.1445810
60. Tsvetkov, N.; Nikolskaia, A.; Shevaleevskiy, O.; et al. TiO_2/halide perovskite interface: The impact of surface state passivation on energy alignment and photovoltaic performance of perovskite solar cells. *Applied Surface Science* 2020, 512, 145666. https://doi.org/10.1016/j.apsusc.2020.145666
61. Mezynska, M.; Brzóska, M.M. Environmental exposure to cadmium—a risk for health of the general population in industrialized countries and preventive strategies. *Environmental Science and Pollution Research* 2018, 25(4), 3211–3232. https://doi.org/10.1007/s11356-017-0827-z
62. Qu, F.; Zheng, W.W. Cadmium Exposure: Mechanisms and Pathways of Toxicity and Implications for Human Health. *Toxics* 2024, 12(6), 388. https://doi.org/10.3390/toxics12060388